

# Unexpected Epitaxial Growth of a Few WS<sub>2</sub> Layers on {1 $\bar{1}$ 00} Facets of ZnO Nanowires

Boris Polyakov,<sup>\*,†</sup> Alexei Kuzmin,<sup>\*,†</sup> Krisjanis Smits,<sup>†</sup> Janis Zideluns,<sup>†</sup> Edgars Butanovs,<sup>†</sup> Jelena Butikova,<sup>†</sup> Sergei Vlassov,<sup>‡</sup> Sergei Piskunov,<sup>†</sup> and Yuri F. Zhukovskii<sup>†</sup>

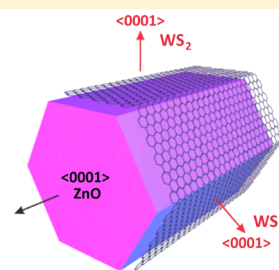
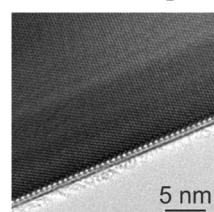
<sup>†</sup>Institute of Solid State Physics, University of Latvia, Kengaraga Street 8, LV-1063 Riga, Latvia

<sup>‡</sup>Institute of Physics, University of Tartu, Ravila 14c, 50412 Tartu, Estonia

## S Supporting Information

**ABSTRACT:** Core-shell nanowires are an interesting and perspective class of radially heterostructured nanomaterials where epitaxial growth of the shell can be realized even at noticeable core-shell lattice mismatch. In this study epitaxial hexagonally shaped shell consisting of WS<sub>2</sub> nanolayers was grown on {1 $\bar{1}$ 00} facets of prismatic wurtzite-structured [0001]-oriented ZnO nanowires for the first time. A synthesis was performed by annealing in a sulfur atmosphere of ZnO/WO<sub>3</sub> core-shell structures, produced by reactive dc magnetron sputtering of an amorphous a-WO<sub>3</sub> layer on top of ZnO nanowire array. The morphology and phase composition of synthesized ZnO/WS<sub>2</sub> core-shell nanowires were confirmed by scanning and transmission electron microscopy (SEM and TEM), micro-Raman, and photoluminescence spectroscopy. Epitaxial growth of WS<sub>2</sub>(0001) layer(s) on {1 $\bar{1}$ 00} facets of ZnO nanowire is unexpected due to incompatibility of their symmetry and structure parameters. To relax the interfacial incoherence, we propose a model of ZnO/WS<sub>2</sub> interface containing WS<sub>2</sub> bridging groups inside and use first-principles simulations to support its feasibility.

Core-shell ZnO/WS<sub>2</sub> nanowire



## 1. INTRODUCTION

Core-shell and multishell nanowires (NWs) are modern types of axially and radially heterostructured nanomaterials intensively explored during the last decades.<sup>1–3</sup> The core-shell approach has several important advantages as compared to conventional two-dimensional (2D) material production technologies: it allows one, for example, to combine materials with lattice mismatch and even to initiate epitaxial growth of shell material on the core template.<sup>1,3,4</sup> As a result, it is possible to significantly improve electrical, mechanical, and optical properties of NWs by proper combination of core and shell materials.<sup>2,5,6</sup> It is worth to mention heterojunction NWs, where p–n junction between core and shell materials turns a core-shell NW into a functional device like a photodetector, LED, nanolaser, etc.<sup>1,2,4,7–9</sup> Therefore, the engineering of core-shell heterostructures opens a new route for creation of novel nanomaterials with advanced properties.

Zinc oxide (ZnO) is among the most thoroughly explored NW materials due to simplicity of its synthesis and a number of beneficial properties.<sup>10</sup> Bulk ZnO is known to be a direct band gap (3.3–3.4 eV) n-type semiconductor.<sup>11</sup> It can be relatively easily grown in a form of NWs<sup>12,13</sup> also at atmospheric pressure.<sup>14</sup> ZnO is known to be a piezoelectric and piezoresistive material; moreover, a piezoelectric nanogenerator prototype, based on zinc oxide NW arrays, was demonstrated several years ago.<sup>15</sup> ZnO NWs are also frequently used as a template for nanomaterials synthesis.<sup>10</sup> Various ZnO/MeS core-shell heterostructures (Me = Pb, Cd, and Zn) were

reported to be used for photovoltaic devices,<sup>16</sup> solar cells,<sup>17</sup> water splitting for hydrogen production,<sup>18,19</sup> high-temperature sensors,<sup>19</sup> and photodetectors.<sup>20,21</sup>

Layered transition metal dichalcogenides such as WS<sub>2</sub> and MoS<sub>2</sub> have attracted recently increasing attention.<sup>22</sup> WS<sub>2</sub> can be produced as thin films, 2D crystals, and nanotubes as well as a component of heterostructures.<sup>23–28</sup> WS<sub>2</sub> is an n-type semiconductor having an indirect band gap  $\Delta\epsilon_{\text{ig}} = 1.3\text{--}1.4$  eV,<sup>29–31</sup> a direct optical band gap  $\Delta\epsilon_{\text{dg}} = 1.7\text{--}1.9$  eV, and strong optical absorption ( $\alpha = 5 \times 10^4$  cm<sup>−1</sup> at 2 eV). Engineering of WS<sub>2</sub> band gap is possible by controlling its thickness from bulk to single layer.<sup>32</sup>

WS<sub>2</sub> is an extremely chemically inert (up to 1000 °C) and nontoxic substance<sup>33</sup> that makes it useful for biomedical applications.<sup>34</sup> It is widely used as a lubricant additive<sup>35</sup> and is studied for applications in lithium-ion batteries<sup>36</sup> and field-effect transistors.<sup>37</sup> Moreover, it can be utilized for solar cells or water splitting due to a good correspondence of its band gap to the solar spectrum.<sup>33,38,39</sup> Enhanced efficiency of H<sub>2</sub>O splitting for hydrogen production by WS<sub>2</sub> was recently demonstrated for heterostructures.<sup>38,40,41</sup> Tahir et al. produced hierarchical WS<sub>2</sub>–ZnO nanocomposites for electronic and photonic applications.<sup>40</sup> Seo et al. synthesized WO<sub>3</sub>–WS<sub>2</sub> heterostructures by

Received: June 17, 2016

Revised: August 11, 2016

Published: August 26, 2016

partial sulfurization of  $\text{WO}_3$  NWs for hydrogen electrocatalysis.<sup>41</sup>

Finally, the use of 2D  $\text{ZnO}$ – $\text{WS}_2$  heterostructures in significantly enhanced ultraviolet (UV) photodetectors was demonstrated recently in ref 42. The heterostructure was produced using a chemical vapor deposition grown monolayer  $\text{WS}_2$  stacked onto the surface of  $\text{ZnO}$  100 nm thin film deposited by magnetron sputtering on glass substrate.<sup>42</sup> In this case, the electron–hole pairs are photogenerated in  $\text{ZnO}$  nanothin film, whereas monolayer  $\text{WS}_2$  functions as a charge transport layer.<sup>42</sup>

In this study, we report for the first time on the epitaxial growth of  $\text{WS}_2$  nanolayers on  $\text{ZnO}$  nanowires. Direct epitaxial growth of  $\text{WS}_2$ (0001) on the  $\{1\bar{1}00\}$  facet of  $\text{ZnO}$  nanowire is unexpected due to incompatibility of their symmetry and structure parameters. To relax the interfacial incoherence we propose a bridge-based model of  $\text{ZnO}/\text{WS}_2$  interface and use first-principles simulations to estimate its feasibility.

## 2. METHODS AND MATERIALS

### 2.1. Synthesis of $\text{ZnO}/\text{WS}_2$ Core–Shell Nanowires.

$\text{ZnO}/\text{WS}_2$  core–shell NWs were produced in three steps: (1)  $\text{ZnO}$  NWs growth on a  $\text{SiO}_2/\text{Si}(100)$  wafer; (2) amorphous  $\text{a-WO}_3$  layer deposition onto  $\text{ZnO}$  NWs; (3)  $\text{ZnO}/\text{WO}_3$  NWs annealing in sulfur atmosphere.

$\text{ZnO}$  NWs were grown by a vapor transport method [also known as atmospheric pressure chemical vapor deposition (APCVD) method] using Au nanoparticles (BBi international, water suspension, 60 nm in diameter) as catalyst via VLS (vapor–liquid–solid growth mechanism).<sup>16</sup> NWs were synthesized on thermally oxidized silicon substrates [ $\text{SiO}_2/\text{Si}(100)$  wafer, Semiconductor Wafer, Inc.] by heating a 1:4 mixture of  $\text{ZnO}$  and graphite powder to 800–900 °C in an open-end quartz tube for 0.5 h. After synthesis samples were studied by scanning electron microscopy (SEM) to confirm successful growth of  $\text{ZnO}$  NWs.

Next,  $\text{ZnO}$  NW samples were coated by a layer of amorphous  $\text{a-WO}_3$ , having a 100 nm thickness on a flat substrate, using reactive dc magnetron sputtering of metallic tungsten target in mixed  $\text{Ar}/\text{O}_2$  atmosphere. The thickness of the  $\text{a-WO}_3$  layer on the surface of  $\text{ZnO}/\text{WO}_3$  NW array on a  $\text{SiO}_2/\text{Si}(100)$  substrate was found to be 10–50 nm as estimated by SEM and transmission electron microscopy (TEM) (see Figure S1 in Supporting Information).

Finally,  $\text{ZnO}/\text{a-WO}_3$  NW samples were annealed in a quartz tube in a sulfur atmosphere during 0.5 h at 800 °C to convert amorphous tungsten trioxide into tungsten sulfide, followed by heating for 0.5 h in inert atmosphere to sublimate some remaining amount of  $\text{WO}_3$ . It is important to note that the growth of the  $\text{WS}_2$  sublayer takes place at the interface between  $\text{ZnO}$  core and  $\text{WO}_3$  shell.

**2.2. Morphological Characterization.** The morphology of  $\text{ZnO}/\text{WS}_2$  core–shell NWs was characterized by a high-resolution SEM focussed ion beam (FIB) electron microscope (Lyra, Tescan). The inner structure of core–shell NWs was revealed using a TEM (Tecnai GF20, FEI) operated at the accelerating voltage of 180 kV.

**2.3. Photoluminescence and Micro-Raman Measurements.** The photoluminescence (PL) measurements were performed at 9 and 300 K using the fourth harmonic (266 nm, or 4.66 eV) of a Nd:YAG laser FQSS266 (CryLas GmbH) as an excitation source. The photoluminescence spectra were

recorded using the Andor Shamrock B-303i spectrograph equipped with a CCD camera (Andor DU-401A-BV).

Micro-Raman and PL spectromicroscopy measurements were performed using a confocal microscope with spectrometer Nanofinder-S (SOLAR TII).<sup>43</sup> A diode-pumped solid-state (DPSS) Nd:YAG laser [ $\lambda = 532$  nm, max continuous wave (cw) power  $P_{\text{ex}} = 150$  mW] was used as the excitation source. A Peltier-cooled back-thinned CCD camera (ProScan HS-101H) was used for detection of Raman and PL spectra. The Hamamatsu R928 photomultiplier tube was employed in confocal-spectral imaging experiments. All measurements were performed in backscattering geometry at room temperature (20 °C) through a Nikon CF Plan Apo 100 $\times$  (NA = 0.95) optical objective.

## 3. THEORETICAL SECTION

**3.1. Motivation of 2D Simulations on  $\text{ZnO}/\text{WS}_2$  Core–Shell Nanowires.** Regular hexagonal prismatic shape of wurtzite-structured NWs, e.g.,  $\text{ZnO}$  NWs synthesized in our experiment,<sup>44</sup> can be formed if the NW axes are oriented along  $[0001]$  crystallographic directions being hollow-centered. Otherwise their symmetry is reduced while stability is lowered.<sup>45</sup> (The symmetry of hexagonally structured  $[0001]$ -oriented  $\text{ZnO}$  NWs can be described by  $P6_3mc$  rod group.) Stability of these NWs can be achieved while they are terminated by lateral facets possessing the smallest surface energy among any wurtzite faces. This requirement is fulfilled for the family of six identical  $(1\bar{1}00)$ ,  $(\bar{1}100)$ ,  $(10\bar{1}0)$ ,  $(\bar{1}010)$ ,  $(01\bar{1}0)$ , and  $(0\bar{1}10)$   $\text{ZnO}$  facets (Figure 1).<sup>46</sup> Alternative  $\{11\bar{2}0\}$  faceting of  $[0001]$ -oriented  $\text{ZnO}$  NW is energetically less favorable.

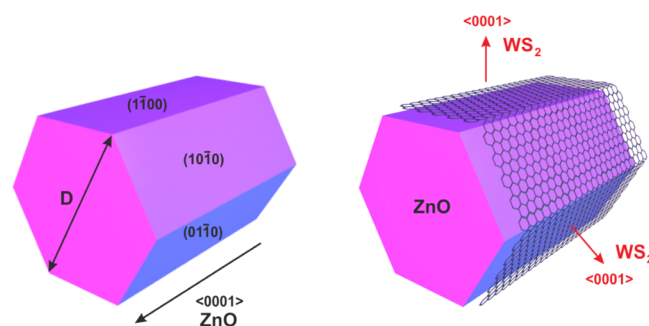


**Figure 1.** Axonometric view of  $\text{ZnO}$   $[0001]$ -oriented nanowire and its lateral facets (left panel), as well as  $\text{ZnO}/\text{WS}_2$  core–shell nanowire (right panel).

Large enough diameters ( $>50$  nm) of  $\text{ZnO}$  NWs synthesized using the CVD method allowed us to assume that the key role in epitaxial  $\text{WS}_2$  layer adhesion to nanowire is played by a family of  $\{1\bar{1}00\}$  plane facets but not by tiny areas around  $\text{ZnO}$  nanowire ribs. This is why the 2D  $\text{ZnO}(1\bar{1}00)/\text{WS}_2$  interface was initially selected for comparison with the experimental data for  $\text{ZnO}/\text{WS}_2$  core–shell NWs. Note that core–shell NWs per se cannot be simulated when using the first-principle theory due to a complexity of their morphology and low symmetry. Therefore, we considered a slab model.

A 20-layer  $\text{ZnO}(1\bar{1}00)$  slab model was chosen for simulations of zinc oxide substrate (thickness of which corresponds to  $[0001]$ -oriented NW possessing diameter of 3.5 nm) and its coverage by  $\text{WS}_2$  nanolayers from both sides. Atomistic models used for simulation of hydrogen molecule

reactivity toward ZnO(1 $\bar{1}$ 00) substrate have been constructed by us recently.<sup>47</sup>

To simulate 2D ZnO/WS<sub>2</sub> core–shell interface, we have established qualitative compatibility between the structures of adsorbent and adsorbate when comparing their bulk morphologies (Figure 2 and Table 1). Note that unit cell of

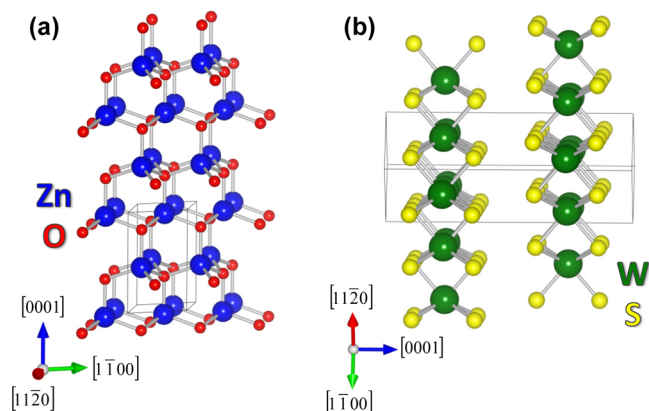


**Figure 2.** Structural parameters of ZnO (a) and WS<sub>2</sub> (b) lattices (small red, medium yellow, medium blue, and large green balls correspond to O, S, Zn, and W atoms, respectively). Light four-faceted prisms correspond to unit cells of ZnO (a) and WS<sub>2</sub> (b) crystals, respectively.

**Table 1.** Comparison of Lattice Parameters and Band Gaps for Bulk WS<sub>2</sub> and ZnO<sup>a</sup>

	WS <sub>2</sub>		ZnO	
	exptl	theory	exptl	theory
$a_0$ (Å)	3.15	3.13	3.25	3.26
$c_0$ (Å)	12.32	12.31	5.21	5.21
$\Delta E_{\text{gap}}$ (eV)	1.3–1.4	2.51	3.3–3.4	3.52

<sup>a</sup>Experimental values are taken from refs 29–31 and 48 for WS<sub>2</sub> and from refs 11, 49, and 50. for ZnO, respectively.

tungsten disulfide contains fragments of two inversely oriented WS<sub>2</sub> layers (Figure 2b). Both structures are described by hexagonal space symmetry groups  $P6_3mc$  (Figure 2a) and  $P6_3/mmc$  (Figure 2b), respectively.

Comparison between the structural parameters of  $a_0$ , and  $c_0$  for ZnO and WS<sub>2</sub> bulk (Figure 2 and Table 1) obtained in calculations and measured experimentally shows their close proximity. This fact enhances the possibility to form a quasi-coherent interface since each  $c_0^{\text{WS}_2} > 2c_0^{\text{ZnO}}$  (resulting in slight bend of WS<sub>2</sub> unit cell contacting to ZnO unit cell), while  $a_0^{\text{ZnO}} \approx a_0^{\text{WS}_2}$ . We have considered both n- and p-type terminations of ZnO(1 $\bar{1}$ 00) slab (Figures S2 and S3 and Table S1 in Supporting Information) although morphology of the former corresponds to a more smooth NW facet observed experimentally.<sup>44</sup> According to conditions of ZnO synthesis described before, we have also constructed slab model of n-type S-doped ZnO(1 $\bar{1}$ 00) substrate where all outer O atoms are substituted by S atoms (Figure S4 and Table S1 in Supporting Information). Other details of models used for ZnO/WS<sub>2</sub> interface are given below and in Supporting Information.

**3.2. Computational Details.** In this study, relaxed 3D models of ZnO and WS<sub>2</sub> lattices (Figure 2) as well as ZnO(1 $\bar{1}$ 00)/WS<sub>2</sub> 2D interfaces were calculated using the periodic hybrid density functional theory (DFT)/Hartree–

Fock (HF) LCAO method. The method utilizes localized Gaussian-type functions (GTFs) in the form of basis set (BS) centered on atomic nuclei for expansion of crystalline orbitals as linear combinations of atomic orbitals, implemented in CRYSTAL14 computer code<sup>51</sup> using the hybrid exchange–correlation functional PBE0.<sup>52,53</sup> For oxygen atoms we used the all-valence BSs of atomic GTFs (constructed using pure s- and hybrid sp-AOs) in the form of 8s-411sp, while for zinc atoms we used the all-valence BS in the form 8s-6411sp-41d as suggested previously.<sup>54</sup> BS for sulfur atoms was adopted in the form of ECP-1111s-1111p-11d,<sup>55</sup> while for tungsten atoms the ECP-11sp-31d<sup>56</sup> BS was used, where ECP is the effective core pseudopotentials employed for acceleration of calculations.

To provide a balanced summation in both direct and reciprocal lattices, the reciprocal space integration was performed by sampling the NW Brillouin zone (BZ) with the 12 × 12 × 1 Monkhorst–Pack mesh<sup>57</sup> that gives in total 16 *k*-points evenly distributed at the BZ. Calculations are considered as converged only when the total energy differs by less than 10<sup>−10</sup> au in two successive cycles of the self-consistent field (SCF) procedure. All the calculations were performed with the total geometry optimization keeping initial symmetry fixed. The optimized geometries of both species were found in a qualitative agreement with those experimentally observed (Table 1). Analogous correlation was observed for electronic properties: the band gap value calculated for bulk ZnO was estimated to be overestimated 3.52 eV versus 3.3–3.4 eV in the experiment,<sup>11,49,50</sup> while for bulk WS<sub>2</sub> the band gap value was found to be 2.31 eV versus 1.3–1.4 eV in the experiment.<sup>29–31</sup> The difference between calculated and experimental values of the band gap for WS<sub>2</sub> is attributed to the incompleteness of the basis set for tungsten used in our hybrid LCAO calculations of its disulfide.

## 4. RESULTS AND DISCUSSION

**4.1. Experimental Data.** TEM images of ZnO/WS<sub>2</sub> core–shell NWs are shown in Figure 3. A gold nanoparticle, located at the end of ZnO NW (Figure 3a), is typical for the most of NWs due to gold-catalyzed VLS growth mechanism. A few layers of WS<sub>2</sub> grown at the ZnO NW surface are well visible as parallel black lines. Their thickness varies in the range of 1–5 monolayers (each of them contains three S–W–S atomic planes). Measured interlayer distance is about 6.0–6.7 Å, which is close to the 6.2–6.4 Å interlayer distance in WS<sub>2</sub> nanostructures.<sup>41,58</sup> It also corresponds to the interlayer distance in WS<sub>2</sub> bulk along the [0001] axis (Figure 2b and Table 1). At high magnification the single-crystalline structure of ZnO NWs is well visible (Figure 3b–d). Measured interplanar distance in core ZnO NWs is equal to 2.8 Å that corresponds to the interval between (1 $\bar{1}$ 00) planes of hexagonal ZnO wurtzite.<sup>59</sup> Selected area electron diffraction (SAED) pattern of ZnO/WS<sub>2</sub> NW is shown in the inset in Figure 3c: its analysis by CrysTBox software<sup>60</sup> gives an evidence of the epitaxial growth WS<sub>2</sub> on top of ZnO core (see Figure S5 in Supporting Information). No other phases (as, for example, ZnS) are observed.

Raman spectroscopy was used to support the formation of WS<sub>2</sub> layers on ZnO NWs. Raman spectra of thin WS<sub>2</sub> nanoplates and ZnO/WS<sub>2</sub> individual NWs, recorded at room temperature, are shown in Figure 4, parts a and b. The Raman spectra of bulk WS<sub>2</sub> and their thickness dependence were interpreted in earlier works.<sup>61–64</sup> Two strongest optical phonon modes<sup>26,65,66</sup> E<sub>2g</sub><sup>1</sup>(Γ) and A<sub>1g</sub>(Γ) were, respectively, detected at



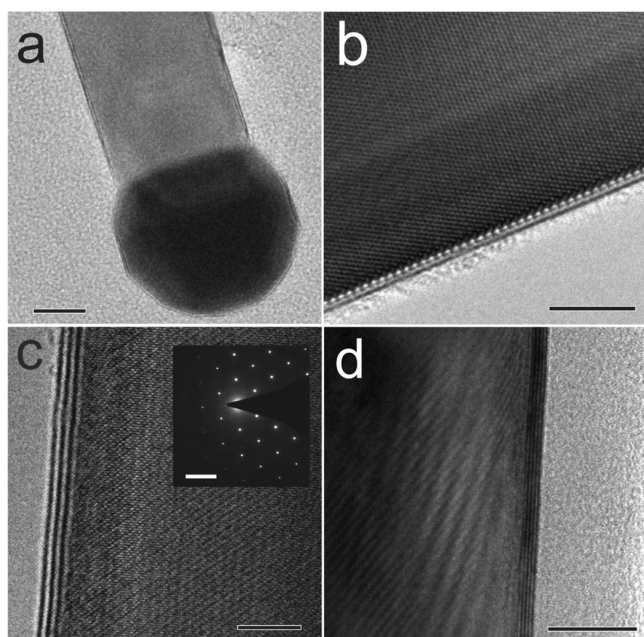


**Figure 3.** TEM images of ZnO/WS<sub>2</sub> core-shell nanowires at small (a) and high magnifications (b–d). The gold nanoparticle at the end of the nanowire is well visible in panel a. Layers of WS<sub>2</sub> are visible as black lines at the ZnO NW surface. The inset in panel c shows the SAED pattern. Scale bars are 20 nm in panel a, 5 nm in panels b–d, and 5 nm<sup>−1</sup> in panel c, inset.

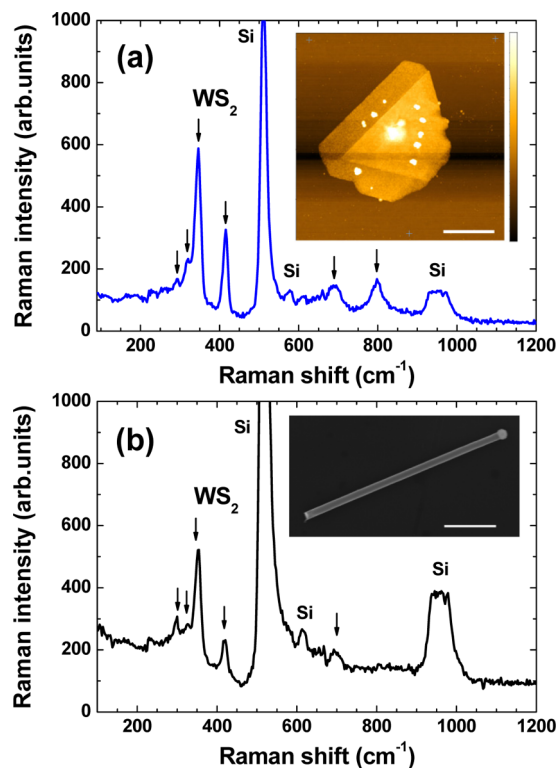


**Figure 4.** (a) Micro-Raman spectrum of WS<sub>2</sub> nanoplate on silicon substrate. Atomic force microscopy (AFM) image of WS<sub>2</sub> nanoplate is shown in the inset (scale bar is 1  $\mu$ m, and color bar is 52 nm). (b) Micro-Raman spectrum of single ZnO/WS<sub>2</sub> NW on silicon substrate. SEM image of the NW is shown in the inset (scale bar is 500 nm). Raman bands of WS<sub>2</sub> phase are indicated by arrows in both images.

347 and 416 cm<sup>−1</sup> in WS<sub>2</sub> nanoplates on silicon wafer and at 354 and 419 cm<sup>−1</sup> in ZnO/WS<sub>2</sub> core-shell NW. These values are close to those of bulk WS<sub>2</sub> (355.5 and 420.5 cm<sup>−1</sup>, respectively).<sup>26</sup> Several weak Raman bands of WS<sub>2</sub> phase were also observed and are indicated by arrows in Figure 4.<sup>26,65,66</sup> The large peak at 521 cm<sup>−1</sup> and its satellite at 959 cm<sup>−1</sup> are the first and second orders of optical mode at  $k = 0$  of the underlying silicon substrate.<sup>67</sup>

Photoluminescence (PL) spectra of pure WS<sub>2</sub>, ZnO, and ZnO/WS<sub>2</sub> NW samples measured at room temperature are shown in Figure 5. WS<sub>2</sub> is expected to transfer from an indirect

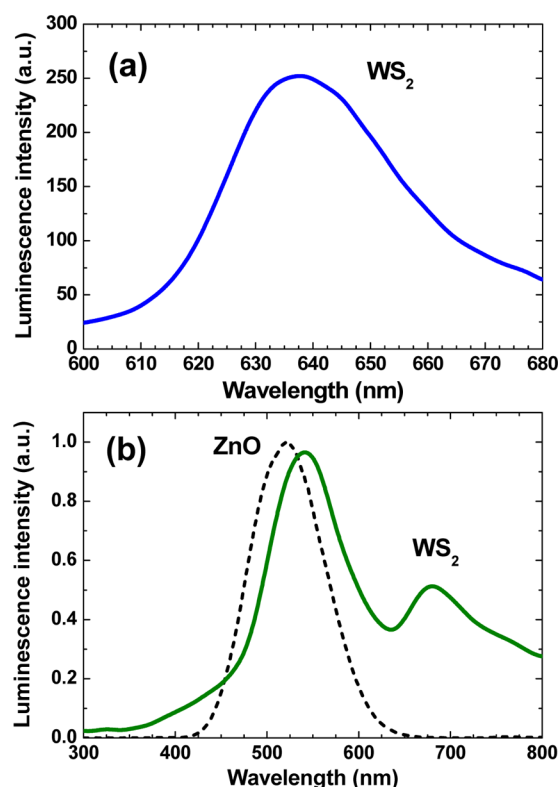


**Figure 5.** Room-temperature photoluminescence spectra of (a) WS<sub>2</sub> islands on a SiO<sub>2</sub>/Si(100) wafer and (b) intact ZnO NWs (dashed curve) and ZnO/WS<sub>2</sub> core-shell NWs (solid curve).

band gap semiconductor in a multilayer form to a direct band gap semiconductor in a few-layer form (ref 26). The broad PL band at 640 nm (Figure 5a) recorded from WS<sub>2</sub> plates by confocal optical microscope corresponds to direct optical band gap of 1.9 eV.<sup>26,68</sup> The PL spectrum of intact ZnO NWs is shown in Figure 5b and has a defect-related band at  $\sim$ 520 nm.<sup>11</sup> The PL spectrum of the ZnO/WS<sub>2</sub> NW array is more complicated and contains emission bands due to ZnO and WS<sub>2</sub> phases (Figure 5b). The emission band at  $\sim$ 540 nm can be attributed to a ZnO core, while PL emission at 680 nm is associated with the WS<sub>2</sub> shell. It is important to note that the ZnO-related band is shifted to longer wavelength compared to intact ZnO NWs. The origin of such shift can be due to electron density redistribution, influence of additional defects, or a formation of ZnS submonolayer. Red shift of the WS<sub>2</sub>-related PL may be caused by influence of the underlying ZnO substrate.<sup>68</sup>

**4.2. Atomistic Prototypes of ZnO/WS<sub>2</sub> Interface to Model Core-Shell Nanowire.** As mentioned in previous section, the interlayer distance in external nanolayers attributed

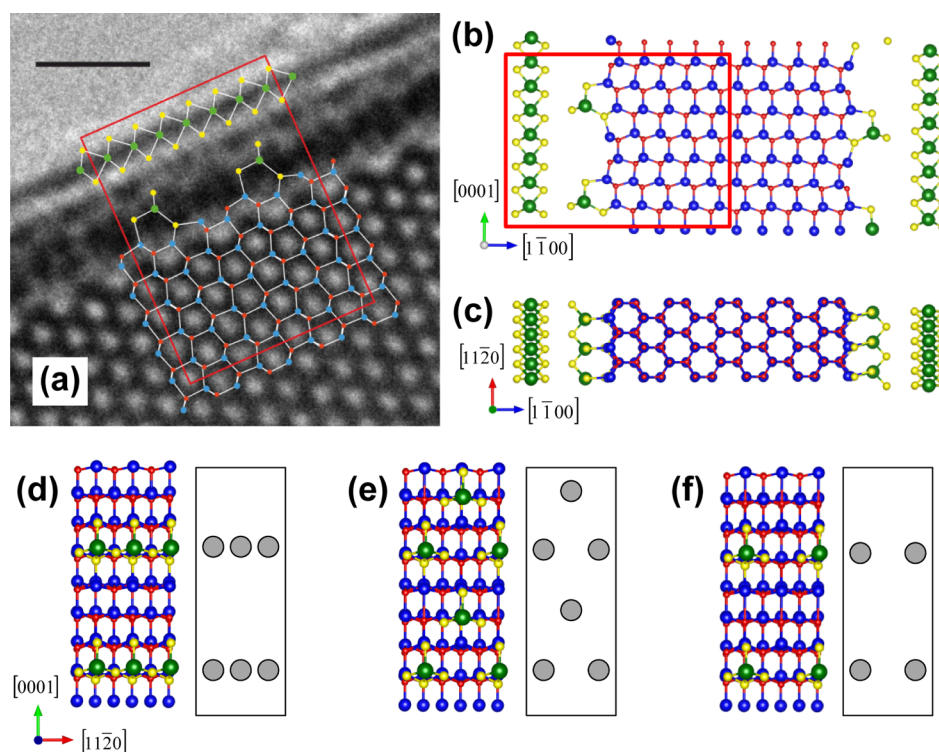


**Figure 6.** (a) Imposition of optimized atomistic model of ZnO( $\bar{1}\bar{1}00$ )/striped 0.5 ML WS<sub>2</sub>( $\bar{1}\bar{1}00$ )/WS<sub>2</sub>(0001) interface on top of the TEM image of ZnO/WS<sub>2</sub> core-shell NW (scale bar is 1 nm) and sections of the same interface across (b) ( $\bar{1}\bar{1}20$ ) and (c) (0001) planes. Three different atomistic models and pictograms of the WS<sub>2</sub> bridging groups atop of the ZnO( $\bar{1}\bar{1}00$ ) surface: (d) striped 0.5 ML, (e) net 0.5 ML, and (f) net 0.25 ML. Gray circles show schematic views of the positions for the WS<sub>2</sub> bridging groups. Atom size and color are the same as in Figure 2. The indexing of axes corresponds to ZnO NW.

to the WS<sub>2</sub>(0001) shell structure is about 6.0–6.7 Å (Figures 3, parts c and d, and 7a–c) which is qualitatively close to the interlayer distances of 6.2–6.4 Å in 2D WS<sub>2</sub> nanostructures (Figure 2b).<sup>41,58</sup> According to TEM observations, the outer WS<sub>2</sub> nanolayers are found to be [0001]-oriented. On the other hand, since ZnO( $\bar{1}\bar{1}00$ ) slab and WS<sub>2</sub>(0001) nanolayer are not spatially and symmetrically compatible (Figure 6a–c), we can insert between them additional 0.5WS<sub>2</sub> striped (Figure 6d), 0.5WS<sub>2</sub> net (Figure 6e), or 0.25WS<sub>2</sub> net (Figure 6f) ( $\bar{1}\bar{1}00$ )-submonolayer, which provides structural relaxation in the two pairs of interfaces, S-doped ZnO( $\bar{1}\bar{1}00$ )/sWS<sub>2</sub>( $\bar{1}\bar{1}00$ ) (Figure 6 and Figures S6–S8 in Supporting Information) and sWS<sub>2</sub>( $\bar{1}\bar{1}00$ )/WS<sub>2</sub>(0001) (Figure 7), which are considered separately. Here *s* denotes the type of inserted submonolayer. This allowed us to preserve periodicity along the ZnO substrate during the structural relaxation of initial geometry. In principle, the intermediate sWS<sub>2</sub>( $\bar{1}\bar{1}00$ ) layer may have a different structure. For example, three possible arrangements of WS<sub>2</sub> groups are shown in Figure 6d–f: these bridging WS<sub>2</sub> groups can form infinite stripes as in Figure 6d, each second WS<sub>2</sub> group in the stripe can be absent as in Figure 6f, which corresponds to regular (net) 0.25 ML, or displaced along the NW direction as in Figure 6e describing regular (net) 0.5 ML. Configurations of WS<sub>2</sub>( $\bar{1}\bar{1}00$ ) submonolayers denoted in Figure 6d–f as adsorbate on ZnO substrate were also recalculated on WS<sub>2</sub>(0001) monolayer as shown in Figure 7a–c. The last two models are likely more favorable for a compensation of structural relaxation in the interface, whereas the model shown in Figure 6d remains strained enough along the [ $\bar{1}\bar{1}00$ ]-oriented WS<sub>2</sub> stripes (Table 2).

Detailed description of n-type S-doped ZnO( $\bar{1}\bar{1}00$ )/sWS<sub>2</sub>( $\bar{1}\bar{1}00$ ) interfaces is given in the next section (Table 2) and in Supporting Information (Figures S6–S8). For comparison, overstrained ZnO( $\bar{1}\bar{1}00$ )/WS<sub>2</sub>( $\bar{1}\bar{1}00$ ) interfaces, both n- and p-types, are considered in Supporting Information (Figures S9 and S10).

Configurations of sWS<sub>2</sub>( $\bar{1}\bar{1}00$ ) submonolayers denoted in Figure 6d–f as adsorbate on ZnO substrate have been also recalculated upon WS<sub>2</sub>(0001) monolayer as shown in Figure 7a–c. The former can be considered as models of a pad between WS<sub>2</sub>(0001) layer and ZnO( $\bar{1}\bar{1}00$ ) core nanowire, which are not spatially and symmetrically compatible. The *x,y* coordinates of W atoms in submonolayers have been frozen when optimizing sWS<sub>2</sub>( $\bar{1}\bar{1}00$ )/WS<sub>2</sub>(0001) interfaces.

**4.3. Results of First-Principles Simulations.** To estimate the interfacial binding energy for 0.25–1 ML WS<sub>2</sub> adsorbate on pure and S-doped ZnO( $\bar{1}\bar{1}00$ ) substrates (see Figures S6–S10, Table 2 and Tables S1 and S2) we have applied the following expression

$$E_{\text{bind}} = 0.5[E_{\text{ZnO}/2\text{WS}_2} - (2E_{\text{WS}_2} + E_{\text{ZnO}})] \quad (1)$$

where  $E_{\text{ZnO}/2\text{WS}_2}$ ,  $E_{\text{WS}_2}$ , and  $E_{\text{ZnO}}$  are the calculated total energies (per unit cell) of the optimized structures for pure or S-doped ZnO slab covered from both sides by WS<sub>2</sub> nanolayers as well as WS<sub>2</sub> nanolayer and pure or S-doped ZnO slab, respectively.

Binding energies per supercell in sWS<sub>2</sub>( $\bar{1}\bar{1}00$ )/WS<sub>2</sub>(0001) interfaces (Figure 7 and Table 3) are estimated according to

$$E_{\text{bind}} = E_{\text{sWS}_2(\bar{1}\bar{1}00)/\text{WS}_2(0001)} - (E_{\text{sWS}_2(\bar{1}\bar{1}00)} + E_{\text{WS}_2(0001)}) \quad (2)$$

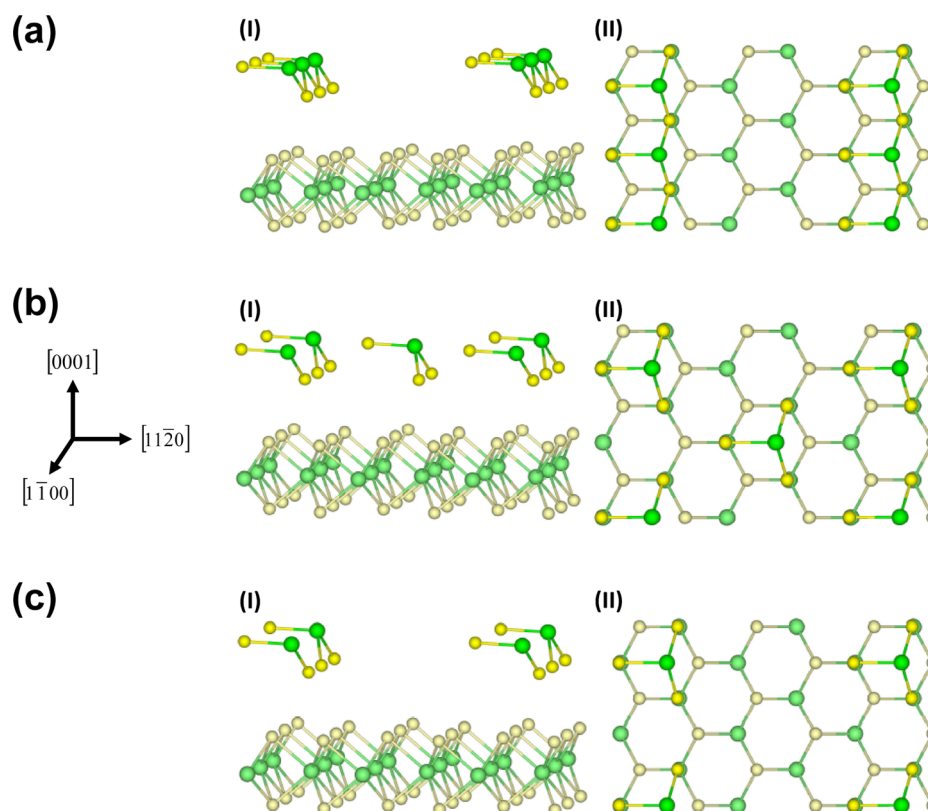


**Figure 7.** Three different arrangements of the  $s\text{WS}_2(1\bar{1}00)$  submonolayer atop  $\text{WS}_2(0001)$  layer: (a) striped  $s = 0.5$  ML, (b) net  $s = 0.5$  ML, and (c) net  $s = 0.25$  ML. They correspond to the images of the same submonolayers atop  $\text{ZnO}(1\bar{1}00)$  substrate in Figure 6d–f. Aside (I) and atop (II) views of  $3 \times 3$  supercells for the  $s\text{WS}_2(1\bar{1}00)/\text{WS}_2(0001)$  interface correspond to n-type morphology of the  $s\text{WS}_2/\text{ZnO}$  interface (Figures S6 and S7). Bright green and bright yellow balls correspond to W and S atoms of the  $(1\bar{1}00)$  submonolayer, while light green and light yellow balls correspond to tungsten and sulfur atoms of the  $(0001)$  monolayer.

**Table 2.** Energy and Geometry Parameters of Optimized  $\text{ZnO}(1\bar{1}00)/s\text{WS}_2$  Interface Models (Figures S6–S8)<sup>a</sup>

models of interface	$E_{\text{bind}}$ (eV)	interlayer distances in substrate (Å)		interfacial distance (Å)	band gap $\Delta\epsilon_g$ (eV)
		$h_{\text{interlayer(outer)}}$	$h_{\text{interlayer(internal)}}$		
striped 0.5 ML	1.59	2.81	2.81	2.16	<i>b</i>
net 0.5 ML	2.21	2.78	2.79	2.15	1.16
net 0.25 ML	2.42	2.73	2.81	2.08	1.61

<sup>a</sup>The total and partial densities of electronic states are shown in Figure S11. <sup>b</sup>Conducting states.

**Table 3.** Energy and Geometry Parameters of Optimized  $\text{WS}_2$  Interface Models  $\text{WS}_2(0001)/\text{WS}_2(0001)$  (Figure 2b) and  $s\text{WS}_2(1\bar{1}00)/\text{WS}_2(0001)$ <sup>a</sup>

models of interface	$E_{\text{bind}}$ (eV)	interlayer distances in $\text{WS}_2$ (Å)		interfacial distance (Å)	band gap $\Delta\epsilon_g$ (eV)
		$h_{\text{W-S external}}$	$h_{\text{W-S internal}}$		
$\text{WS}_2(0001)/\text{WS}_2(0001)$	0.04	1.56	3.11	6.15	2.70
striped $0.5\text{WS}_2(1\bar{1}00)/\text{WS}_2(0001)$	0.08	1.54	3.09	5.95	1.61
net $0.5\text{WS}_2(1\bar{1}00)/\text{WS}_2(0001)$	0.41	1.47	3.09	5.91	2.47
net $0.25\text{WS}_2(1\bar{1}00)/\text{WS}_2(0001)$	0.58	1.44	3.10	5.82	2.51

<sup>a</sup>The total and partial densities of electronic states are shown in Figure S12.

where  $E_{s\text{WS}_2(1\bar{1}00)/\text{WS}_2(0001)}$ ,  $E_{s\text{WS}_2(1\bar{1}00)}$ , and  $E_{\text{WS}_2(0001)}$  are the calculated total energies (per unit cell) of the optimized structures of interface and both its constituents, respectively.

As compared to the initial interface configurations determined by the morphology of  $\text{ZnO}$  substrate, the optimized structures of  $\text{ZnO}(1\bar{1}00)/s\text{WS}_2$  do not changed drastically (Tables 2 and S2), except for noticeable increase of  $h_{\text{interlayer(outer)}}$  compared to the corresponding distance in the

outer and internal layers of zinc oxide slabs (Table S1). On the other hand, this interlayer  $(1\bar{1}00)$  distance is well-correlated with the experimental value (2.8 Å) found by TEM (Figure 3).

Comparison of results obtained for three  $\text{ZnO}(1\bar{1}00)/s\text{WS}_2$  interface configurations (Table 2 and Figures S6–S8) clearly shows lower stability of their striped configuration shown in Figure 6d as compared to both net configurations (Figure 6, parts e and f). Thus, the former is hardly to be realized. When



decreasing the concentration of WS<sub>2</sub> bridging groups their strain as well as interfacial distance to substrate also decrease.

Analogously with energy parameters for ZnO(1̄100)/sWS<sub>2</sub> interface configurations, the results were also obtained for sWS<sub>2</sub>(1̄100)/WS<sub>2</sub>(0001) interfaces. Table 3 provides information on the binding energy  $E_{\text{bind}}$  between the two layers [for WS<sub>2</sub>(0001)/WS<sub>2</sub>(0001) and three types of sWS<sub>2</sub>(1̄100)/WS<sub>2</sub>(0001) interfaces], the band gap  $\Delta\epsilon_g$  and geometry parameters (interlayer and interfacial distances). Note that the low value of the binding energy for WS<sub>2</sub>(0001)/WS<sub>2</sub>(0001) interface agrees well with that obtained by plane wave calculations.<sup>69</sup> The results reported in Table 3 indicate lower stability of the striped configuration shown in Figure 7a as compared to both net configurations (Figure 7, parts b and c). When decreasing the concentration of WS<sub>2</sub> bridging groups their strain as well as interfacial distance to (0001) substrate also decrease. Thus, considering models for both constituents of ZnO(1̄100)/sWS<sub>2</sub>(1̄100)/WS<sub>2</sub>(0001) interface observed experimentally we can suppose that they are more stable and less strained for net 0.25 and 0.5 ML configurations.

## 5. CONCLUSIONS

An epitaxial shell consisting of a WS<sub>2</sub> nanolayer was grown on ZnO NW core for the first time using the specific procedure. An amorphous layer of WO<sub>3</sub> was deposited on ZnO NW array and converted into WS<sub>2</sub> in a sulfur atmosphere at 800 °C. Typical thickness of the WS<sub>2</sub> shell was found to be 1–5 monolayers. The formation of the WS<sub>2</sub> phase was confirmed by TEM studies as well as by Raman scattering and optical spectroscopy. Atomic arrangement of WS<sub>2</sub> layer on the ZnO(1̄100) facets in different possible configurations as well as various structural and electronic properties of ZnO/WS<sub>2</sub> interface were clarified using large-scale first-principles calculations. We have constructed models of ZnO(1̄100)/sWS<sub>2</sub>(1̄100) interfaces, both pure and S-doped, as well as a justified model of WS<sub>2</sub>(0001)/sWS<sub>2</sub>(1̄100) interface where sWS<sub>2</sub>(1̄100) submonolayer bridging structures serve as pads between experimentally observed WS<sub>2</sub>(0001) shell nanolayers and ZnO(1̄100) substrate. Intermediate interfacial WS<sub>2</sub>-containing and {1̄100}-oriented submonolayers are more stable when their quasimolecular groups are separated by at least next-neighboring distances which reduce essentially the strain of WS<sub>2</sub>(0001) shells. We have found qualitative agreement in estimate of interplanar interface distance when comparing experimental and theoretical results and provided an explanation for strong adhesion of WS<sub>2</sub> nanolayer to ZnO substrate.

## ■ ASSOCIATED CONTENT

### ■ Supporting Information

The Supporting Information is available free of charge on the ACS Publications website at DOI: 10.1021/acs.jpcc.6b06139.

Characterization of ZnO/WO<sub>3</sub> core–shell nanowires by TEM, results of selected area electron diffraction for ZnO/WS<sub>2</sub> core–shell nanowire, theoretical atomistic models of ZnO(1̄100) substrates with various morphologies, sWS<sub>2</sub>/S-covered ZnO(1̄100) core–shell interfaces and the model of WS<sub>2</sub> monolayer coverage of pristine ZnO(1̄100) substrate as well as the electronic density of states for ZnO(1̄100) and WS<sub>2</sub>(0001) substrates and ZnO(1̄100)/sWS<sub>2</sub> or sWS<sub>2</sub>(1̄100)/WS<sub>2</sub>(0001) interfaces (PDF)

## ■ AUTHOR INFORMATION

### Corresponding Authors

\*E-mail: boris.polyakov@cfi.lu.lv. Phone: +371-67187511. Fax: +371-67132778.

\*E-mail: a.kuzmin@cfi.lu.lv. Phone: +371-67251691. Fax: +371-67132778.

### Notes

The authors declare no competing financial interest.

## ■ ACKNOWLEDGMENTS

The present research was supported by the Latvian National Research Program IMIS2. S.P. and Y.F.Z. are grateful to the ERA.Net RUS Plus WATERSPLIT project no. 237 for the financial support. S.V. acknowledges the support of the project IUT2-25.

## ■ REFERENCES

- (1) Li, Y.; Qian, F.; Xiang, J.; Lieber, C. M. Nanowire electronic and optoelectronic devices. *Mater. Today* **2006**, *9*, 18–27.
- (2) Yan, R.; Gargas, D.; Yang, P. Nanowire photonics. *Nat. Photonics* **2009**, *3*, 569–576.
- (3) Kempa, T. J.; Day, R. W.; Kim, S.-K.; Park, H.-G.; Lieber, C. M. Semiconductor nanowires: a platform for exploring limits and concepts for nano-enabled solar cells. *Energy Environ. Sci.* **2013**, *6*, 719–733.
- (4) Dong, Y.; Tian, B.; Kempa, T. J.; Lieber, C. M. Coaxial group III-nitride nanowire photovoltaics. *Nano Lett.* **2009**, *9*, 2183–2187.
- (5) Lauhon, L. J.; Gudiksen, M. S.; Wang, D.; Lieber, C. M. Epitaxial core-shell and core-multishell nanowire heterostructures. *Nature* **2002**, *420*, 57–61.
- (6) Vlassov, S.; Polyakov, B.; Dorogin, L. M.; Vahtrus, M.; Mets, M.; Antsov, M.; Saar, R.; Romanov, A. E.; Löhms, A.; Löhms, R. Shape restoration effect in Ag-SiO<sub>2</sub> core-shell nanowires. *Nano Lett.* **2014**, *14*, 5201–5205.
- (7) Qian, F.; Li, Y.; Gradecak, S.; Park, H.; Dong, Y.; Ding, Y.; Wang, Z. L.; Lieber, C. M. Multi-quantum-well nanowire heterostructures for wavelength-controlled lasers. *Nat. Mater.* **2008**, *7*, 701–706.
- (8) Zhai, T.; Fang, X.; Liao, M.; Xu, X.; Zeng, H.; Yoshio, B.; Golberg, D. A comprehensive review of one-dimensional metal-oxide nanostructure photodetectors. *Sensors* **2009**, *9*, 6504–6529.
- (9) Tian, W.; Lu, H.; Li, L. Nanoscale ultraviolet photodetectors based on one-dimensional metal oxide nanostructures. *Nano Res.* **2015**, *8*, 382–405.
- (10) Wang, Z. L. ZnO nanowire and nanobelt platform for nanotechnology. *Mater. Sci. Eng., R* **2009**, *64*, 33–71.
- (11) Özgür, U.; Alivov, Y. I.; Liu, C.; Teke, A.; Reshchikov, M. A.; Doğan, S.; Avrutin, V.; Cho, S.-J.; Morkoç, H. A comprehensive review of ZnO materials and devices. *J. Appl. Phys.* **2005**, *98*, 041301.
- (12) Lee, W.; Jeong, M.-C.; Myoung, J.-M. Catalyst-free growth of ZnO nanowires by metal-organic chemical vapour deposition (MOCVD) and thermal evaporation. *Acta Mater.* **2004**, *52*, 3949–3957.
- (13) Chang, C.-W.; Wu, H.-T.; Huang, S.-H.; Chen, C.-K.; Un, I.-W.; Yen, T.-J. Single-crystalline heterostructure of ZnO nanowire arrays on large Ag microplates and its photocatalytic activity. *Acta Mater.* **2013**, *61*, 6993–6999.
- (14) Huang, M. H.; Wu, Y.; Feick, H.; Tran, N.; Weber, E.; Yang, P. Catalytic growth of zinc oxide nanowires by vapor transport. *Adv. Mater.* **2001**, *13*, 113–116.
- (15) Wang, Z. L.; Song, J. Piezoelectric nanogenerators based on zinc oxide nanowire arrays. *Science* **2006**, *312*, 242–246.
- (16) Zhu, Y. F.; Zhou, G. H.; Ding, H. Y.; Liu, A. H.; Lin, Y. B.; Dong, Y. W. Synthesis and characterization of highly-ordered ZnO/PbS core/shell heterostructures. *Superlattices Microstruct.* **2011**, *50*, 549–556.
- (17) Guerguerian, G.; Elhordoy, F.; Pereyra, C. J.; Marotti, R. E.; Martin, F.; Leinen, D.; Ramos-Barrado, J. R.; Dalchiele, E. A. ZnO

nanorod/CdS nanocrystal core/shell-type heterostructures for solar cell applications. *Nanotechnology* **2011**, *22*, 505401.

(18) Wang, X.; Liu, G.; Lu, G. Q.; Cheng, H. M. Stable photocatalytic hydrogen evolution from water over ZnO-CdS core-shell nanorods. *Int. J. Hydrogen Energy* **2010**, *35*, 8199–8205.

(19) Fang, X.; Zhai, T.; Gautam, U. K.; Li, L.; Wu, L.; Bando, Y.; Golberg, D. ZnS nanostructures: From synthesis to applications. *Prog. Mater. Sci.* **2011**, *56*, 175–287.

(20) Hu, L.; Yan, J.; Liao, M.; Xiang, H.; Gong, X.; Zhang, L.; Fang, X. An optimized ultraviolet - a light photodetector with wide-range photoresponse based on ZnS/ZnO biaxial nanobelt. *Adv. Mater.* **2012**, *24*, 2305–2309.

(21) Zhang, F.; Ding, Y.; Zhang, Y.; Zhang, X.; Wang, Z. L. Piezophototronic effect enhanced visible and ultraviolet photodetection using a ZnO-CdS core-shell micro/nanowire. *ACS Nano* **2012**, *6*, 9229–9236.

(22) Duan, X.; Wang, C.; Pan, A.; Yu, R.; Duan, X. Two-dimensional transition metal dichalcogenides as atomically thin semiconductors: opportunities and challenges. *Chem. Soc. Rev.* **2015**, *44*, 8859–8876.

(23) Tenne, R. Inorganic nanotubes and fullerene-like nanoparticles. *Nat. Nanotechnol.* **2006**, *1*, 103–111.

(24) Scharf, T.; Prasad, S.; Dugger, M.; Kotula, P.; Goeke, R.; Grubbs, R. Growth, structure, and tribological behavior of atomic layer-deposited tungsten disulfide solid lubricant coatings with applications to MEMS. *Acta Mater.* **2006**, *54*, 4731–4743.

(25) Morrish, R.; Haak, T.; Wolden, C. A. Low temperature synthesis of n-type WS<sub>2</sub> thin films via H<sub>2</sub>S plasma sulfurization of WO<sub>3</sub>. *Chem. Mater.* **2014**, *26*, 3986–3992.

(26) Gutierrez, H. R.; Perea-Lopez, N.; Elias, A. L.; Berkdemir, A.; Wang, B.; Lv, R.; Lopez-Urias, F.; Crespi, V. H.; Terrones, H.; Terrones, M. Extraordinary room-temperature photoluminescence in WS<sub>2</sub> triangular monolayers. *Nano Lett.* **2013**, *13*, 3447–3454.

(27) Gong, Y.; Lin, J.; Wang, X.; Shi, G.; Lei, S.; Lin, Z.; Zou, X.; Ye, G.; Vajtai, R.; Yakobson, B. I.; et al. Vertical and in-plane heterostructures from WS<sub>2</sub>/MoS<sub>2</sub> monolayers. *Nat. Mater.* **2014**, *13*, 1135–1142.

(28) Sheng, Y.; Xu, W.; Wang, X.; He, Z.; Rong, Y.; Warner, J. H. Mixed multilayered vertical heterostructures utilizing strained monolayer WS<sub>2</sub>. *Nanoscale* **2016**, *8*, 2639–2647.

(29) Kam, K. K.; Parkinson, B. A. Detailed photocurrent spectroscopy of the semiconducting group VIB transition metal dichalcogenides. *J. Phys. Chem.* **1982**, *86*, 463–467.

(30) Kuc, A.; Zibouche, N.; Heine, T. Influence of quantum confinement on the electronic structure of the transition metal sulfide TS<sub>2</sub>. *Phys. Rev. B: Condens. Matter Mater. Phys.* **2011**, *83*, 245213.

(31) Braga, D.; Gutiérrez Lezama, I.; Berger, H.; Morpurgo, A. F. Quantitative determination of the band gap of WS<sub>2</sub> with ambipolar ionic liquid-gated transistors. *Nano Lett.* **2012**, *12*, 5218–5223.

(32) Long, H.; Tao, L.; Tang, C. Y.; Zhou, B.; Zhao, Y.; Zeng, L.; Yu, S. F.; Lau, S. P.; Chai, Y.; Tsang, Y. H. Tuning nonlinear optical absorption properties of WS<sub>2</sub> nanosheets. *Nanoscale* **2015**, *7*, 17771–17777.

(33) Jager-Waldau, A.; Lux-Steiner, M. C.; Bucher, E. WS<sub>2</sub> thin films: a new candidate for solar cells. *Preprint 23th IEEE Photovoltaic Specialist Conf.* **1993**, 1–6.

(34) Yong, Y.; Zhou, L.; Gu, Z.; Yan, L.; Tian, G.; Zheng, X.; Liu, X.; Zhang, X.; Shi, J.; Cong, W.; et al. WS<sub>2</sub> nanosheet as a new photosensitizer carrier for combined photodynamic and photothermal therapy of cancer cells. *Nanoscale* **2014**, *6*, 10394–10403.

(35) Ratoi, M.; Niste, V. B.; Walker, J.; Zekonyte, J. Mechanism of action of WS<sub>2</sub> lubricant nanoadditives in high-pressure contacts. *Tribol. Lett.* **2013**, *52*, 81–91.

(36) Rui, X.; Tan, H.; Yan, Q. Nanostructured metal sulfides for energy storage. *Nanoscale* **2014**, *6*, 9889–9924.

(37) Iqbal, M. W.; Iqbal, M. Z.; Khan, M. F.; Shehzad, M. A.; Seo, Y.; Eom, J. Deep-ultraviolet-light-driven reversible doping of WS<sub>2</sub> field-effect transistors. *Nanoscale* **2015**, *7*, 747–757.

(38) Yan, Y.; Xia, B.; Li, N.; Xu, Z.; Fisher, A.; Wang, X. Vertically oriented MoS<sub>2</sub> and WS<sub>2</sub> nanosheets directly grown on carbon cloth as

efficient and stable -dimensional hydrogen-evolving cathodes. *J. Mater. Chem. A* **2015**, *3*, 131–135.

(39) Sang, Y.; Zhao, Z.; Zhao, M.; Hao, P.; Leng, Y.; Liu, H. From UV to near-infrared, WS<sub>2</sub> nanosheet: A novel photocatalyst for full solar light spectrum photodegradation. *Adv. Mater.* **2015**, *27*, 363–369.

(40) Tahir, M. N.; Yella, A.; Therese, H. A.; Mugnaioli, E.; Panthofer, M.; Khan, H. U.; Knoll, W.; Kolb, U.; Tremel, W. Synthesis of hierarchically grown ZnO@NT-WS<sub>2</sub> nanocomposites. *Chem. Mater.* **2009**, *21*, 5382–5387.

(41) Seo, B.; Jeong, H. Y.; Hong, S. Y.; Zak, A.; Joo, S. H. Impact of a conductive oxide core in tungsten sulfide-based nanostructures on the hydrogen evolution reaction. *Chem. Commun.* **2015**, *51*, 8334–8337.

(42) Lan, C.; Li, C.; Wang, S.; Yin, Y.; Guo, H.; Liu, N.; Liu, Y. ZnO-WS<sub>2</sub> heterostructures for enhanced ultra-violet photodetectors. *RSC Adv.* **2016**, *6*, 67520–67524.

(43) Kuzmin, A.; Kalendarev, R.; Kursitis, A.; Purans, J. Confocal spectromicroscopy of amorphous and nanocrystalline tungsten oxide films. *J. Non-Cryst. Solids* **2007**, *353*, 1840–1843.

(44) Polyakov, B.; Dorogin, L.; Lohmus, A.; Romanov, A.; Lohmus, R. In situ measurement of the kinetic friction of ZnO nanowires inside a scanning electron microscope. *Appl. Surf. Sci.* **2012**, *258*, 3227–3231.

(45) Evarestov, R. A. *Theoretical Modeling of Inorganic Nanostructures. Symmetry and ab-initio Calculations of Nanolayers, Nanotubes and Nanowires*; Springer-Verlag: Berlin-Heidelberg, Germany, 2015.

(46) Zhukovskii, Y. F.; Piskunov, S.; Lisovski, O.; Spohr, E.; Evarestov, R. A. Quantum chemical simulations of doped ZnO nanowires for photocatalytic hydrogen generation. *Phys. Status Solidi B* **2016**, DOI: 10.1002/pssb.201600452.

(47) Usseinov, A. B.; Kotomin, E. A.; Akilbekov, A. T.; Zhukovskii, Y. F.; Purans, J. Hydrogen induced metallization of ZnO(1100) surface: Ab initio study. *Thin Solid Films* **2014**, *553*, 38–42.

(48) Schutte, W.; De Boer, J. L.; Jellinek, F. Crystal structures of tungsten disulfide and diselenide. *J. Solid State Chem.* **1987**, *70*, 207–209.

(49) Abrahams, S. C.; Bernstein, J. L. Remeasurement of the structure of hexagonal ZnO. *Acta Crystallogr., Sect. B: Struct. Crystallogr. Cryst. Chem.* **1969**, *25*, 1233–1236.

(50) Karzel, H.; Potzel, W.; Köfferlein, M.; Schiessl, W.; Steiner, M.; Hiller, U.; Kalvius, G. M.; Mitchell, D. W.; Das, T. P.; Blaha, P.; et al. Lattice dynamics and hyperfine interactions in ZnO and ZnSe at high external pressures. *Phys. Rev. B: Condens. Matter Mater. Phys.* **1996**, *53*, 11425–11438.

(51) Dovesi, R.; Saunders, V. R.; Roetti, C.; Orlando, R.; Zicovich-Wilson, C. M.; Pascale, F.; Civalieri, B.; Doll, K.; Harrison, N. M.; Bush, I. J.; D'Arco, P.; et al. *CRYSTAL14 User's Manual*; University of Torino: Torino, Italy, 2014.

(52) Perdew, J. P.; Ernzerhof, M.; Burke, K. Rationale for mixing exact exchange with density functional approximations. *J. Chem. Phys.* **1996**, *105*, 9982–9985.

(53) Adamo, C.; Barone, V. Toward reliable density functional methods without adjustable parameters: The PBE0 model. *J. Chem. Phys.* **1999**, *110*, 6158–6170.

(54) Gryaznov, D.; Blokhin, E.; Sorokine, A.; Kotomin, E.; Evarestov, R.; Bussmann-Holder, A.; Maier, J. A comparative ab initio thermodynamic study of oxygen vacancies in ZnO and SrTiO<sub>3</sub>: Emphasis on phonon contribution. *J. Phys. Chem. C* **2013**, *117*, 13776–13784.

(55) Bandura, A. V.; Evarestov, R. A. Structure and stability of SnS<sub>2</sub>-based single- and multi-wall nanotubes. *Surf. Sci.* **2015**, *641*, 6–15.

(56) Corà, F.; Patel, A.; Harrison, N. M.; Dovesi, R.; Catlow, C. R. A. An ab initio Hartree-Fock study of the cubic and tetragonal phases of bulk tungsten trioxide. *J. Am. Chem. Soc.* **1996**, *118*, 12174–12182.

(57) Monkhorst, H. J.; Pack, J. D. Special points for Brillouin-zone integrations. *Phys. Rev. B* **1976**, *13*, 5188–5192.

(58) Krause, M.; Mucklich, A.; Zak, A.; Seifert, G.; Gemming, S. High resolution TEM study of WS<sub>2</sub> nanotubes. *Phys. Status Solidi B* **2011**, *248*, 2716–2719.



- (59) Wang, W.; Wang, L.; Liu, L.; He, C.; Tan, J.; Liang, Y. Morphology-controlled synthesis and growth mechanism of ZnO nanostructures via the NaCl nonaqueous ionic liquid route. *CrystEngComm* **2012**, *14*, 4997–5004.
- (60) Klinger, M.; Jäger, A. Crystallographic Tool Box (CrysTBox): automated tools for transmission electron microscopists and crystallographers. *J. Appl. Crystallogr.* **2015**, *48*, 2012–2018.
- (61) Sourisseau, C.; Cruege, F.; Fouassier, M.; Alba, M. Second-order Raman effects, inelastic neutron scattering and lattice dynamics in 2H-WS<sub>2</sub>. *Chem. Phys.* **1991**, *150*, 281–293.
- (62) Berkdemir, A.; Gutierrez, H. R.; Botello-Mendez, A. R.; Perea-Lopez, N.; Elias, A. L.; Chia, C.-I.; Wang, B.; Crespi, V. H.; Lopez-Urias, F.; Charlier, J.-C.; et al. Identification of individual and few layers of WS<sub>2</sub> using Raman Spectroscopy. *Sci. Rep.* **2013**, *3*, 1755.
- (63) Mitiglu, A. A.; Plochocka, P.; Deligeorgis, G.; Anghel, S.; Kulyuk, L.; Maude, D. K. Second-order resonant Raman scattering in single-layer tungsten disulfide WS<sub>2</sub>. *Phys. Rev. B: Condens. Matter Mater. Phys.* **2014**, *89*, 245442.
- (64) Liang, L.; Meunier, V. First-principles Raman spectra of MoS<sub>2</sub>, WS<sub>2</sub> and their heterostructures. *Nanoscale* **2014**, *6*, 5394–5401.
- (65) Molina-Sanchez, A.; Wirtz, L. Phonons in single-layer and few-layer MoS<sub>2</sub> and WS<sub>2</sub>. *Phys. Rev. B: Condens. Matter Mater. Phys.* **2011**, *84*, 155413.
- (66) Peimyoo, N.; Shang, J.; Yang, W.; Wang, Y.; Cong, C.; Yu, T. Thermal conductivity determination of suspended mono- and bilayer WS<sub>2</sub> by Raman spectroscopy. *Nano Res.* **2015**, *8*, 1210–1221.
- (67) Parker, J. H.; Feldman, D. W.; Ashkin, M. Raman scattering by silicon and germanium. *Phys. Rev.* **1967**, *155*, 712–714.
- (68) Xu, Z. Q.; Zhang, Y.; Lin, S.; Zheng, C.; Zhong, Y. L.; Xia, X.; Li, Z.; Sophia, P. J.; Fuhrer, M. S.; Cheng, Y. B.; et al. Synthesis and transfer of large-area monolayer WS<sub>2</sub> crystals: Moving toward the recyclable use of sapphire substrates. *ACS Nano* **2015**, *9*, 6178–6187.
- (69) He, J.; Hummer, K.; Franchini, C. Stacking effects on the electronic and optical properties of bilayer transition metal dichalcogenides MoS<sub>2</sub>, MoSe<sub>2</sub>, WS<sub>2</sub>, and WSe<sub>2</sub>. *Phys. Rev. B: Condens. Matter Mater. Phys.* **2014**, *89*, 075409.